scientific reports

Check for updates

OPEN

Si wafers unpredictable inhomogeneities and their crucial role in porous Si fabrication

Guido Mula[1]✉, Muhammad Naseem Akhtar[1], Francesca Assunta Pisu[1], Giuseppe Leonetti[2]✉, Bruno Torre[2], Luca Boarino[2] & Eleonora Cara[2]

Porous Silicon (PSi) is a remarkably versatile material, whose structural reproducibility is highly sensitive to substrate properties and fabrication parameters. This study demonstrates that persistent inconsistencies in PSi fabrication originate not from experimental errors, but from undetected nanoscale substrate inhomogeneities that elude standard metrology. We identify these features as small-scale inhomogeneities occurring at densities as high as 8×10^8 cm^{-2}, representing a nine-orders-of-magnitude increase over the industrial defect standards. Scanning Electron Microscopy and Kelvin Probe Force Microscopy (KPFM) were employed to probe these fluctuations, establishing a detection threshold for both defect density and charge carriers concentration fluctuations and confirming that such defects remain hidden to high-end surface metrology while critically impacting electrochemical etching. We propose that the observed morphology distortions probably result from a localized modulation of the depletion region and a consequent redirection of the tunneling current. Our results highlight how these unpredictable inhomogeneities dictate the local transition from ordered vertical growth to stochastic branched structures. Furthermore, we propose Electrochemical NanoLithography (ENL) as a high-sensitivity diagnostic tool to map these defects, enabling the efficient selection of optimal and homogeneous wafers. By ensuring substrate consistency, this approach significantly enhances the reliability of experimental data and paves the way for the successful transition of PSi technologies from laboratory research to large-scale industrial applications.

Keywords Porous silicon, Bulk Si inhomogeneities, Porosity, Doping

Abbreviations

CZ	Czochralski method
EC	Electrochemical
ENL	Electrochemical NanoLithography
FEG	Field emission gun
FFT	Fast fourier transform
FZ	Float Zone method
KPFM	Kelvin Probe Force Microscopy
PSi	Porous silicon
SEM	Scanning electron microscopy

Silicon technology is at the foundation of almost all modern technological advancement, from nanoelectronics[1,2] to battery electrodes[3–7] to photovoltaics[8] and many more. At the origin of most of these applications are Si wafers, usually monocrystalline Si, with various crystalline orientations, doping levels and dopant species. Although for most applications the main requirements are surface flatness, choice of the dopants, average doping level and crystal orientation[9], there is a growing concern about the reproducibility of the Si ingots from which the Si wafers are cut. However, even the best high-quality Si wafers are not as homogeneous as many usually imagine, as clearly indicated in Si wafer sellers' indications[10]. For instance, point defects in Czochralski Si wafers have been intensely studied[11–13]. Some research results indicate that thermal annealing can lead to improved wafers' behavior[11] and in some cases those defects are considered useful for stopping the propagation

[1]PoroSiLab, Dipartimento di Fisica, Università degli Studi di Cagliari, Cittadella Universitaria di Monserrato, S.P. 8 Km 0.700, Monserrato I-09024, CA, Italy. [2]Advanced Materials Metrology and Life Sciences Division, INRiM (Istituto Nazionale di Ricerca Metrologica), Strada delle Cacce 91, Torino 10135, TO, Italy. ✉email: guido.mula@unica.it; g.leonetti@inrim.it

of dislocations when depositing epitaxial layers[14]. Because of issues related to these defects, in microelectronics there is a growing interest towards wafers having an epitaxial top layer, which guarantees improvements over defects density, structural defects and dopant homogeneity and control[15]. Many manufacturers have epitaxial wafers on their websites and suggests them for specific applications[16,17].

As a general rule, most users assume that nominally identical Si wafers are interchangeable regardless of the producer or the wafer's lot. This approach however overlooks significant variations in homogeneity and reproducibility that are a major challenge for fabricating nanostructured Si-based materials, such as PSi materials and devices.

There is a huge number of studies devoted to methods to improve Si ingots homogeneity, in particular from the point of view of various kinds of defects[18,19] and dopant distribution[20,21]. Most Si wafers are produced by Czochralski[22] and Float-Zone[23] methods, where many features such as vibrations, temperature gradients, rotation and pulling speeds, become crucial in the final result[24,25].

In this work, first we will briefly discuss the main production methods for Si wafers, underlining the main causes leading to the formation of defects, the strategies for solving the different issues, and what relevant issues remain. Then, we will go through a demonstration of how even almost undetectable wafer inhomogeneities, as can be very small-scale impurities/dopants concentration fluctuations, can lead nominally identical wafers to give dramatically different results in the electrochemical fabrication of PSi and other top-down fabrication methods where doping conditions are crucial. The implications of these differences in the reproducibility of the results are especially relevant for the PSi community, and we will demonstrate how our patented method Electrochemical NanoLithography (ENL)[26,27] is able to put into evidence the presence of localized small-size defects in wafer lots and thus evaluate the wafers' bulk homogeneity. While the ENL method cannot specifically identify the source of these defects, it reliably detects their presence.

Si wafers fabrication methods

In view of the understanding of the impact of the irregularities of the Si wafers on the PSi formation processes and why achieving homogeneous Si wafers if far from straightforward, it is worth spending a few words on the most common methods used for Si wafers production. Many methods are available for the growth of single-crystal materials[28], and a very interesting panorama of these methods can be found in a recent publication by Robert S. Feigelson[29], where the author depicts a broad selection of crystal growth strategies divided into growth from melt, solutions, and vapor. These methods apply to a wide variety of materials, including but not limited to group IV elements such as Ge[30] and Si[31], compounds from III-V group, as GaAs[32] and GaN[33] or II-VI group, as ZnSe[34] and CdTe[35]. An overview of the topic can be found, among many, in the 2014 book by G. Müller[36]. As just discussed, many compounds can be obtained as wafers and, in the case of Si technology, the need of high-quality, single-crystal, reproducible substrate material has restricted the choice essentially to methods exploiting a molten material. Among them, the most common methods for obtaining monocrystalline Si wafers are by far Czochralski[22] and Float-Zone[37]. Both methods start with the original idea by Jan Czochralski[22,38] that single crystals can be obtained starting from a crystalline seed that, when put into contact with a melt in controlled conditions, will initiate the crystallization of the Si ingot with the same orientation as the seed. A schematic of these two methods is shown in Fig. 1.

Czochralski method

The Czochralski method (CZ) starts from the melting of pure Si pieces in a crucible, generally a quartz crucible, where dopant impurities can be added to obtain p- or n-doped ingots (Fig. 1a). Many factors will affect the

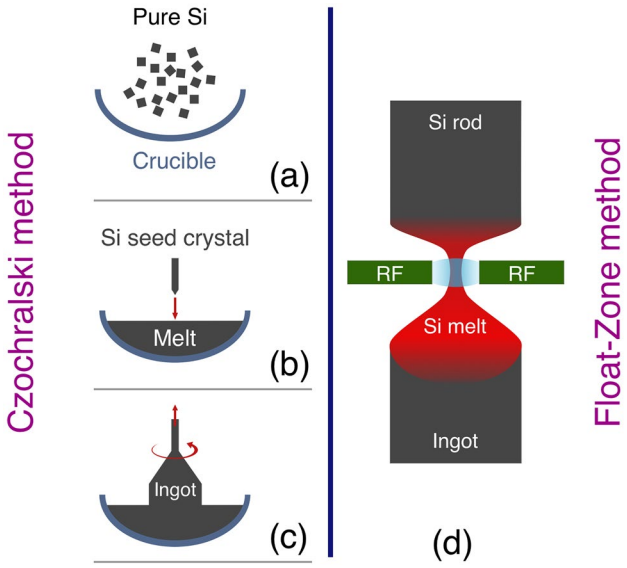


Fig. 1. Schematic of a Czochralski (left) and a Float-Zone (right) processes.

achievement of a high-quality crystal. During the fabrication process, the crystalline seed is first dipped (Fig. 1b) and then pulled away while rotating at a constant speed[39] (Fig. 1c). The rotation and the pulling speeds are critical factors for an optimized crystallization of Si from the melt[39]. However, the crystal formation is also very sensitive to vibrations[40], justifying the need for seismographers to check the stability during the ingot formation. If such vibrations occur, the affected part of the ingot is marked and then removed from the ingot at the end of the fabrication process. Another issue is related to the solubility limit of the dopants[41–43]. The solubility is quite sensitive to the temperature[41,42], and this implies that the cooling ramp constitutes a critical component to control the homogeneity of the final product[44], especially for the larger wafers (present perspectives are oriented towards 40 cm diameter ingots[45], while largest commercial wafers are usually 30 cm diameter[46,47]).

Given the temperature inhomogeneities and the dependence of the dopants' solubility limit on that parameter, a resistivity difference along the ingot length and radius is expected. In Fig. 2a a schematic of the resistivity variations that can be expected along the radius and the length of a Si ingot is shown. An experimental measurement of these inhomogeneities is available in the work by S. Dubois et al.[21], while in Fig. 2b a photograph of a PSi layer fabricated on a 2 inch n^{++} Si wafer is shown, where the presence of ring defects is revealed by the colored rings. Please note that in that case the rings are not centered on the wafer's axis.

Rings are a well-known problem of ingot formation, and reports of methods to possibly limit this issue are regularly published[48,49]. Rings are often evidenced even when the wafers are cut from the ingot[50]. These inhomogeneities are on a relatively large scale and are less prone to interfere at the nanoscale with the Si wafer nanoscale processing, but their existence leads to significant effects, as we will describe in this work, and is far from being negligible for the fabrication of homogeneous PSi samples on large surfaces.

Another significant issue affecting crystal formation in the CZ method is related to vortex and fluid movements within the melt that, for large ingots, can even be turbulent. The stabilization of the molten material is the topic of many studies that investigate how different parameters (e.g. gravity) can affect the fluid movement. To take care of this, a relatively common method is the exploitation of magnetic fluid confinement[51]. Many different geometries have been investigated, making the control of the melt by means of a magnetic field a method that has proved to effectively limit turbulence and improve the wafers homogeneity, although without fully avoiding the presence of rings and similar inhomogeneities. Other issues with the CZ method are related to the oxygen release from the crucible, the presence of carbon impurities and thermal defects[52].

Float-zone method

The Float-Zone method (FZ), schematically represented in Fig. 1d, is quite different from CZ. Instead of using a crucible as in CZ fabrication, FZ starts from a solid feeding rod that is locally melted usually by radiofrequency or local heating. As in CZ, FZ also uses a crystalline seed to control the orientation of the formed crystalline ingot, but in this case the molten zone is small and moving upward, while the crystal is forming downward[53]. With respect to CZ, in FZ the lack of a crucible in contact with the melt significantly lowers the impurity concentration in the final ingot, thanks to the absence of impurities coming from the crucible[54]. Many manufacturers, in their websites[55,56] or in their application notes[57,58], compare CZ and FZ methods, given their high interest and their relevance in the Si wafer domain.

Comparison and present strategies

The CZ and FZ methods have both advantages and limits, some of them already discussed above. As a general rule, CZ wafers are cheaper than FZ and allow for higher throughput and a higher versatility in the dopant introduction within the melt[55,56]. FZ method allows for higher purity, given by the lack of crucible, and has a

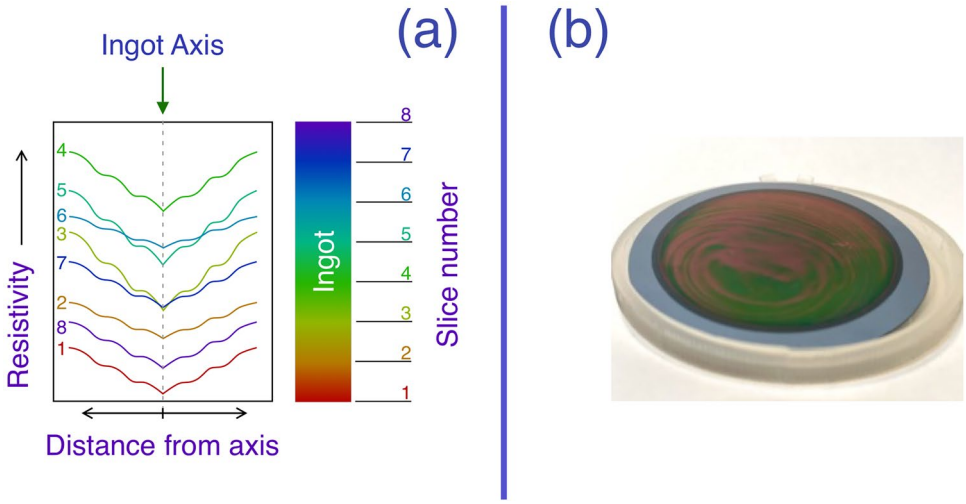


Fig. 2. (**a**) Schematic of resistivity inhomogeneities along a CZ-grown Si ingot. Radial and axial inhomogeneities are clearly evidenced. (**b**) Picture of a PSi layer formed using a 2-inch highly doped Si wafer. The dopant element is Phosphorus, the resistivity 3–7 mOhm·cm. The inhomogeneity rings are clearly visible.

better crystal quality with respect to CZ. With respect to CZ, FZ has a limitation in the maximum diameter of the Si ingot induced by the surface tension of the mold. Up to 200 mm is considered the maximum possible FZ ingot diameter, a factor that strongly limits the applicability of the method to industrial applications where large wafers are required. As an indication, CZ wafers are studied for wafers of 400 mm diameter[45,58], while the most recent results for FZ are about strategies for 300 mm diameter ingots[54].

An interesting strategy for an improved homogeneity of phosphorus-doped Si wafers is the neutron transmutation doping[59–61], a method used also for other materials, as GaN[62]. This method is based on the neutron irradiation of Si ingots where[30] 30Si atoms capture a neutron and next decay into[31] P atoms. This doping method allows for significantly improved doping homogeneity, but at the same time is considerably more expensive and time consuming.

This quick overview clearly shows the complexity of the Si wafers fabrication process, explains why there are inhomogeneities that at present are still not fully controlled, and it underlines the relevance of a better understanding of the CZ fabrication process, the most common fabrication method, to move towards Si wafers whose homogeneity is highly controlled on all length scales. This understanding necessarily comes from improved detection of wafers' defects and of differences among wafers' lots.

Experimental details

Porous silicon fabrication

PSi layers are formed by a constant-current electrochemical etching of highly doped Si wafers, using an HF-based ethanoic electrochemical solution. The details of our fabrication method are described elsewhere[63–65]. The control of the pores distribution is achieved by using our patented Electrochemical NanoLithography (ENL) technique[26,27], an easy and scalable lithographic method designed to separately control the density and the distribution of the pores independently of the formation parameters used for the pores' fabrication. PSi layers were fabricated on several lots of n^+ phosphorus-doped Si substrates from INSETO (UK). All wafers were (100) oriented and had a resistivity in the 12–15 mΩ·cm. The etching current density was varied in the 70–1200 mA/cm^2, while the HF concentration was varied in the 15–35% v/v starting from a 50% HF/H_2O RPE commercial solution and EtOH RPE, both from Carlo Erba (Italy).

Structural characterization

The structural characterization was carried out by using FEI Inspect F™ Scanning Electron Microscope with Field Emission Gun (SEM-FEG) and a FEI Quanta 3D™ FEG dual beam microscope, both operating at 30 kV and equipped with secondary electron Everhart–Thornley detectors. Top view images were acquired in the center of the samples and in further two equally-spaced points for the small dimension samples and in five points for the bigger ones. A magnification of 60,000 × was exploited to acquire the pore distribution and dimensions for the subsequent Fast fourier transform (FFT) analysis. Cross-sectional analysis was performed by cutting each sample by half along the diameter line of the porous area with the assistance of a diamond engraver. The samples were observed in correspondence of the same top-view areas exploiting a 90° SEM specimen stub with a tilting angle of 5°.

Kelvin Probe Force Microscopy (KPFM)

We used an MFP/3D Oxford instrument-Asylum research Atomic Force Microscope (AFM), capable of performing Kelvin Probe Force Microscopy (KPFM) measurements, equipped with ASYELEC01.R2 Ti/Ir coated commercial AFM tips (Oxinst/Asylum research), having typical curvature radius of 25 nm, nominal spring constant 2.8 N/m and resonance frequency of 75 kHz. Second pass is performed at an elevation $\Delta z = 50$ nm with respect to the surface, to optimize the tradeoff between lateral resolution and image stability. For these measurements we obtained a sensitivity and accuracy of 4 meV, assessed on a freshly doped HOPG reference sample, and a lateral resolution better then 50 nm. During all the measurements relative humidity was reduced below 3% to avoid humidity contribution in the electrical measurements.

KPFM measurements relay on a standard two pass technique in which the first pass is used to acquire surface topography in standard AC mode and the second one repeat the topography on the same line with an additional elevation Δz from the surface to probe long range forces at a constant distance from the surface. During the second pass the tip oscillation is induced applying an AC voltage between the tip and the sample, while a DC bias is adjusted by an external feedback loop to compensate and measure the local contact potential difference between tip and sample[66]. As result a map of the contact potential of the substrate is collected in parallel to the topographic map allowing correlating and disclosing the influence of topography and composition on the position of the Fermi level at the nanoscale. Typical energy resolution of this technique lays in the meV range while lateral resolution, arising from the cooperative contribution of the tip curvature radius and the elevation Δz is typically in the 30–50 nm range, in environmental conditions. These measurements have been widely used to investigate compositional uniformity and charge distributions in semiconductor applications such as dopant homogeneity at the surface. Henning et al.[67] evaluated that a change in 1 meV in a contact potential allowed resolving changes in dopant concentration of +/- 5% in the vicinity of 10^{14} cm^{-3}, and +/- 8% in the vicinity of 10^{18} cm^{-3} at the surface doped Si samples.

Results and discussion

Electrochemical signature – large-scale inhomogeneities

For the fabrication of PSi on Si dies taken from a large wafer, a common good practice shared with the PSi community is to keep track of the position within the wafer of various pieces. This is of course a valid approach since, as we already discussed, the wafers are far from being perfectly homogeneous in terms of defects or doping

level. An example is shown in Fig. 2b for a 2-inch diameter PSi layer. Spatial variations in wafer properties result in a measurable electrochemical signature when the porous layer is fabricated under constant-current conditions, as shown in Fig. 3. This behavior is consistent regardless of the Si wafer manufacturer, as it stems from the intrinsic large-scale inhomogeneity of the dopant distribution we already discussed.

In a constant-current porous layer fabrication process, the voltage evolution is related to the progressive stabilization of the electrochemical (EC) etching process: if the process is fully stable, the applied voltage remains constant. However, the initial stages of the pores nucleation and propagation always show a transient phase that, as shown in Fig. 3, varies from sample to sample. These transient gradients can be mitigated by fabricating and subsequently removing a sacrificial layer (a few hundred nanometers thick) using a 0.5 M NaOH aqueous solution or a similar etching agent. This approach effectively removes the impurities deriving from the wafer manufacturing (such as slicing and polishing of CZ-grown ingots) and reduces the amplitude of the gradients.

While the use of a sacrificial layer improves the PSi fabrication process when the inhomogeneities arise from the surface treatments, in particular those used during the wafer fabrication processes, it has no effect on small-scale bulk impurity. Our results show that for wafers affected by these small-scale inhomogeneities these transients remain almost unaffected regardless of the thickness of the sacrificial layer.

Porous structure characterization – small-scale inhomogeneities

The fabrication process of PSi layers depends heavily on both EC etching parameters and substrate properties[68], as we described earlier. The EC corrosion starts where the surface shows random small deviations from planarity that locally enhance the electric field and therefore favor the initiation of the EC pore nucleation process. The same is of course valid within the bulk material while the pore fabrication process is ongoing, where local modifications of the carrier density or of the electric field control the electrochemical etching path.

The scale at which these inhomogeneities play a relevant role for EC processes strongly depends on the pore diameter. As a matter of fact, large pores exhibit low sensitivity to minor fluctuations, while small pores are significantly more responsive as is apparent from the well-known experimental shape of PSi nano-, meso- and macro-pores, where the dendritic structure progressively disappears with increasing pore diameter[69]. This is schematically shown in Fig. 4, for (a) the path of a single pore having a diameter comparable with the inhomogeneities size, (b) the irregularities of a PSi layer when the pore diameter is comparable with the defects' size and (c) the regular formation of a PSi layer when the inhomogeneities length-scale is significantly smaller than the average pore size.

Detecting bulk Si defects by using electrolytical methods has a long history[70,71]. Both with or without chemical treatments of the Si surfaces, the idea is that the electrochemical processes are sensitive to bulk Si quality and defects alter the process. Therefore, these studies show that an appropriate strategy aimed at highlighting those alterations can avoid multiple complex characterization steps. However, existing chemical and EC methods have mainly identified defects whose size is orders of magnitude larger than a PSi mesopore. Our approach proposes the use of Electrochemical NanoLithography[26,27] (ENL) to extend the principles behind these strategies to the nanoscale, a length range hardly accessible by standards EC-based methods. ENL bridges then the gap between μm-scale EC methodologies and the nanoscale, offering a versatile sub-100 nm approach to wafer analysis. In addition, its scalability offers the prospective of its use for large-scale wafer characterization.

In agreement with this choice, all our samples were prepared by using ENL to form controlled surface indentations. This bilayer-based approach provides independent control over pore density and distribution, as schematically illustrated in Fig. 5. The method consists of a sacrificial bilayer where the top layer, L1, acts as a density control step and the second layer, L2, acts as an order control step. Chemically removing these two layers leaves indentations on the surface that will act as seeds for the subsequent fabrication of a new porous layer.

The well-known large differences in the structure of PSi pores with different diameters[68] is a demonstration of the behavior shown in Fig. 4a,c and highlights the sensitivity of the pore fabrication process to the substrate quality. In Fig. 6, we show an SEM cross-section of a mesoporous PSi layer obtained from a n^+-doped Si substrate

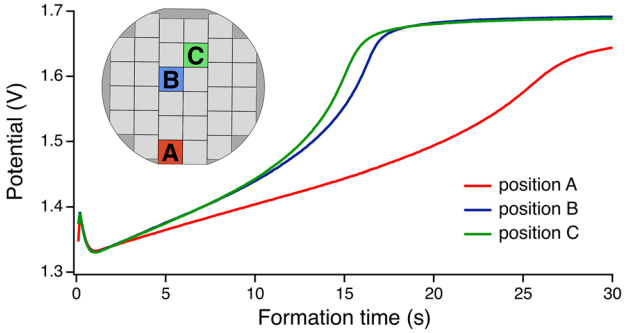


Fig. 3. Time evolution of applied voltage in a constant-current PSi fabrication process using a highly As-doped 10 cm diameter Si wafers from Si Materials for three different pieces. The position of each piece on the wafer is shown in the inset. The same behavior is observed when using wafers with other dopants, doping levels and producers. For this wafer and these PSi fabrication processes, the HF concentration was 15%, the current density 75 mA/cm^2, the substrate resistivity in the 3–7 mΩ cm range. The PSi layer thickness was ∼1.3 μm for all samples.

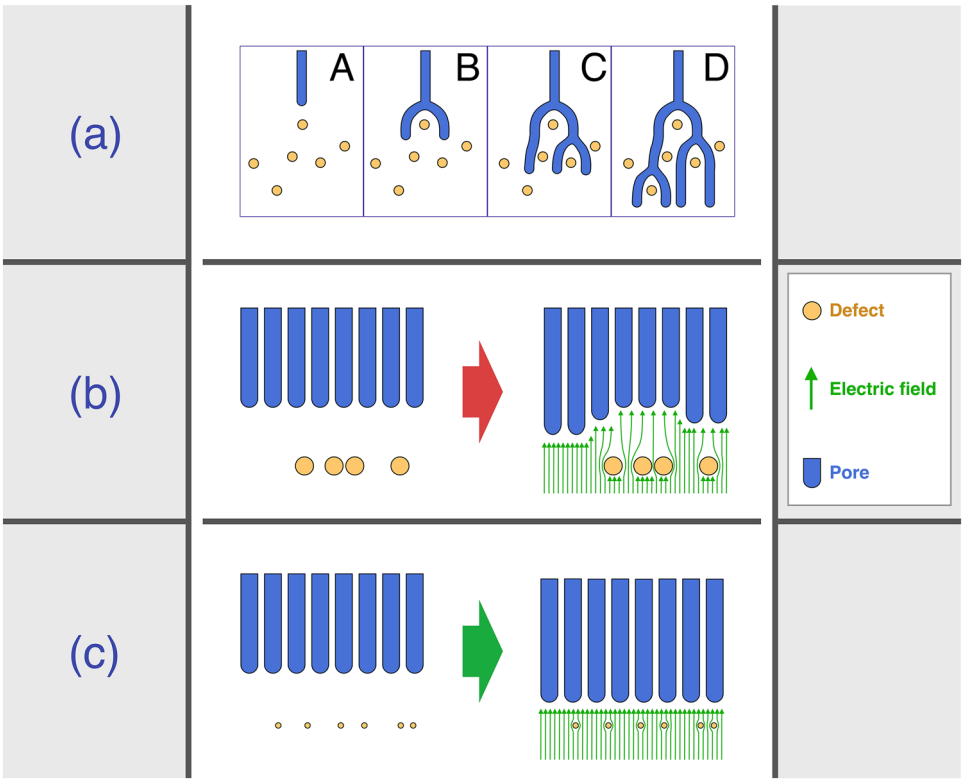


Fig. 4. Schematic of the length-scale related effect of inhomogeneities/defects on the pore propagation process. (**a**) path modification along a single pore propagation process induced by the defect presence: if pore diameters are at the same scale as the inhomogeneities, the pore propagation will be strongly affected by the consequent electric field inhomogeneities; (**b**) Perturbations on a PSi layer induced by inhomogeneities having the same length scale as the pore diameter: the pore-defect size coincidence induces a high sensitivity to local defects and inhomogeneities of the whole layer. (**c**) PSi layer is progressively less affected as the pore diameter exceeds the inhomogeneities length-scale.

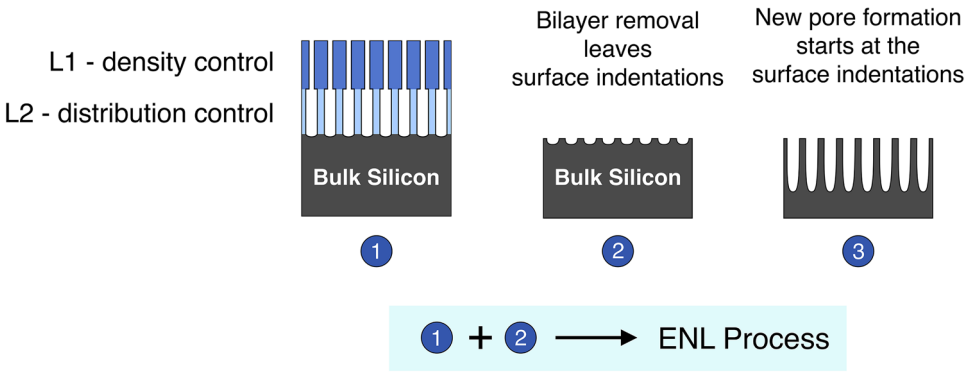


Fig. 5. Schematic of the ENL process[26,27]. (1) Formation of the sacrificial bilayer (L1 + L2); (2) removal of the sacrificial bilayer to reveal surface indentations; (3) growth of the target porous layer guided by the pre-patterned indentations.

using HF 25% v/v, $i = 600$ mA/cm^2, t = 1,0 s and HF 22% v/v, $i = 900$ mA/cm^2, t = 0,5 s for the two sacrificial layers L1 and L2, and HF 22% v/v, $i = 900$ mA/cm^2, t = 2,0 s for the layer imaged. In Fig. 6, small-scale inhomogeneities are clearly visible. The dramatic deviation of the pores' direction from the expected one is apparent and clearly indicates the presence of substrate inhomogeneities that strongly affects the electrochemical etching process. This kind of layer inhomogeneities necessarily affects the properties of the PSi layer, making research results unreliable due to random substrate defects rather than insufficient process control.

Figure 7 shows the cross-section of another PSi sample, fabricated on a similar substrate using the same parameters for the sample in Fig. 6, where the dramatic change in the pore shape induced by the bulk Si

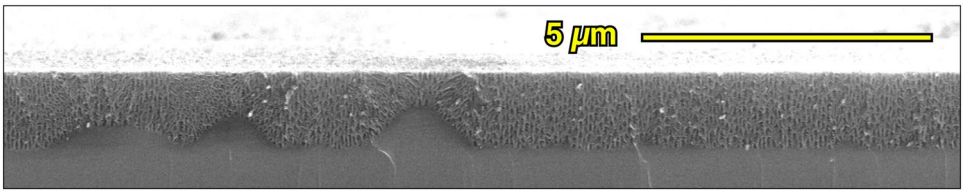


Fig. 6. Strong irregularities in a mesoporous PSi layer induced by small-scale bulk n^+-type Si inhomogeneities.

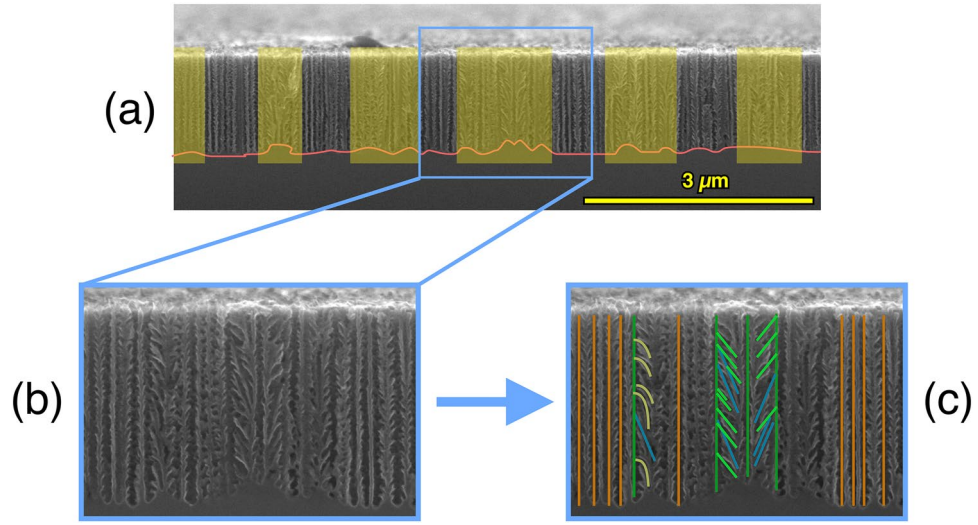


Fig. 7. SEM cross-section of an n^+-type PSi layer. (**a**) Overview of the porous layer, where the yellow shaded areas highlight the zones of defective pores propagation. The red profile highlights the resulting irregular growth front, that is the interface between porous and bulk Si. (**b**) The pore irregularities are evidenced for one of the irregular pore formation areas of (**a**). (**c**) The irregular pores' trajectories and branching (blue and green lines) of defective areas are evidenced and compared with the shape of regular pores (orange vertical lines).

irregularities is evidenced. Although we do not see the pyramidal defects of Fig. 6, the large irregularities in the pore shapes are nonetheless clearly visible. In Fig. 7a the yellow rectangles highlight the almost regular spacing within defective pores portions. The shape of irregular pores is clearly visible in Fig. 7b and further evidenced in Fig. 7c.

In Fig. 8 we show the comparison of SEM cross sections of (top) a sample fabricated on an inhomogeneous substrate and (bottom) a sample fabricated on a homogeneous substrate. The sample on top is the same shown in Fig. 7, while the one on the bottom is fabricated on a 2″ wafer using an etching solution with HF 22% v/v for all processes, $i = 900$ mA/cm^2, $t = 1{,}6$ s and $i = 1060$ mA/cm^2, $t = 1.2$ s, respectively, for the two sacrificial ENL layers L1 and L2, while $i = 1060$ mA/cm^2, $t = 2.0$ s for the layer shown. Other current density values gave similar results in terms of defects densities, but the pores structure itself may differ given its strong dependence on the current density. There is a striking difference in the porous structure homogeneity in the two samples, and the interface between the porous layer and the bulk Si is significantly affected by the presence of these inhomogeneities. The substrates are nominally identical, and the formation parameters are essentially the same in both cases, so that the comparison highlights the different behavior of the two lots. The use of different HF concentrations for the L1 layer in the two samples (25% *vs.* 22%) has no impact on the subsequent formation of the third layer: the ENL protocol is specifically optimized to ensure inter-layer integrity and to prevent artifacts related to solution switching, such as electrolyte infiltration or surface drying issues. Please note that the local irregularities and branching observed at the microscopic level (Fig. 7) translate into a non-uniform growth front at larger scales, as clearly demonstrated by the comparison between inhomogeneous and homogeneous substrates shown in Fig. 8.

The scale of these inhomogeneities makes them extremely difficult to detect, since characterization tools able to detect such defects are either with excellent spatial resolution but insufficient chemical resolution (such as, e.g., Scanning and/or Transmission Electron Microscopy or Electron Tomography) or with excellent chemical resolution but insufficient spatial resolution (e.g. Secondary Ion Mass Spectroscopy or Rutherford Backscattering). We will go into further detail in section "KPFM measurements".

In Fig. 9 are compared the SEM top views of PSi layers formed after ENL processing using an inhomogeneous substrate (left) and a homogeneous one (right). The inhomogeneities we've seen in cross-section in Fig. 7 and Fig. 8 are apparent in the left image, where the irregular pores in the sacrificial double layer led to a lack of pore nucleation below those irregularities. Please note that the spacing between irregular pores observed in the cross

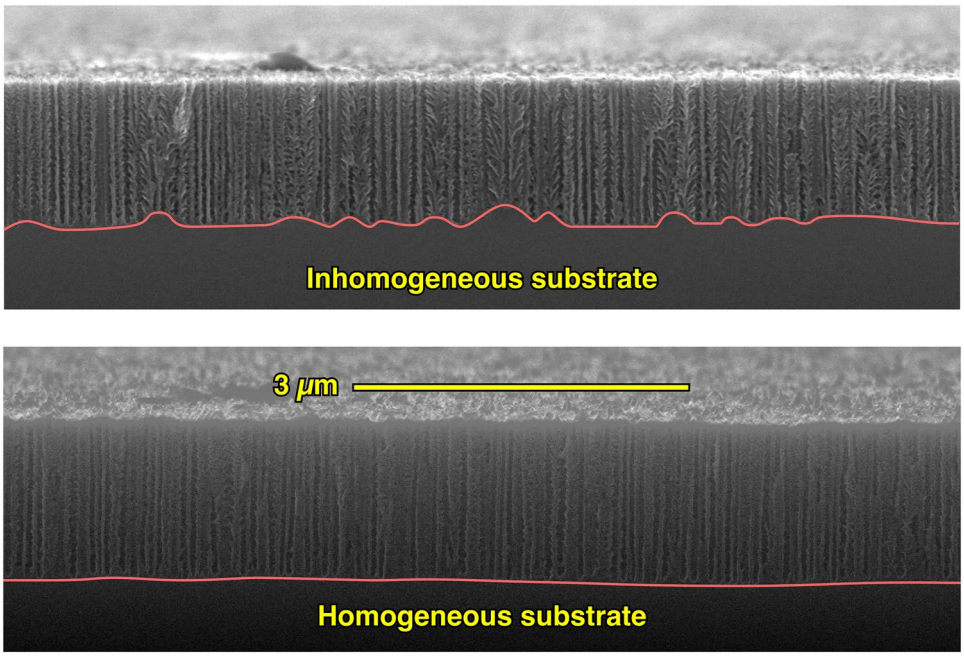


Fig. 8. Comparison of the SEM cross section of PSi layers fabricated using an inhomogeneous substrate (**a**) and a homogeneous substrate (**b**). The PSi/bulk Si interface is highlighted. The sample shown in (**a**) is the same as Fig. 7.

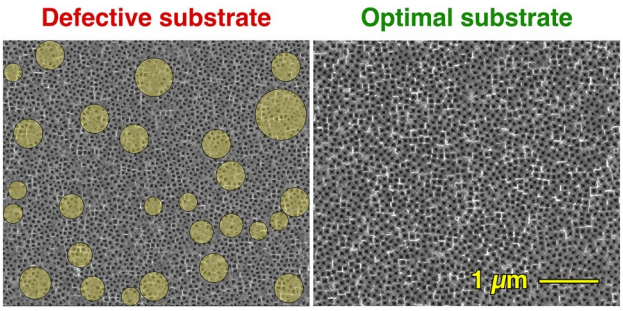


Fig. 9. Top-view SEM comparison of two PSi layers formed using identical electrochemical parameters after ENL processing. Left: defective substrate. The yellow shaded circles highlight regions where the substrate inhomogeneities suppress or distort the pore formation process. Right: optimal substrate. No defective areas are present.

section is visible also in the top view. These defects are totally absent when the Si substrate used is homogeneous, as shown in Fig. 9 right. These results further demonstrate how ENL acts as a powerful diagnostic tool, since it effectively "maps" the substrate defects appearing as localized areas with irregular or even absent pore formation.

From top view SEM imaging we can evaluate the density of these inhomogeneities by counting them on various surface areas. In Fig. 10, we show the top view SEM images from three samples from three different wafer lots having the same resistivity range. All samples were prepared using the same ENL processing, with the aim of analyzing samples having a controlled distribution of surface indentations. For additional clarity, panels (a) and (b) show the thresholded SEM images of a defective (a) and of an optimal (b) substrate's surface, where the defective areas are identified by the almost complete absence of pores. In (a) a red circle indicates one of such areas. Coherently, the red circles in the other top-panel higher-resolution images highlight the defective areas, while the light green circles in the bottom lower resolution images highlight the defective areas for counting. The measured surface density reflects the defect density observed in cross section and the defective areas are easily identified by relevant changes in the pores' structure (from clustered small spots to lack of pore nucleation) that are absent in optimal-quality samples. It easy to see how, going from left to right, the number of defective areas decreases.

Rough estimates on the three lots indicate that the defect density is ≈8 defects/μm^2 for sample in (c, d), 1–2 defects/μm^2 for sample in (e, f) and no visible defects for sample in (g, h). Please note that the pore size depends on the PSi fabrication parameters and not on the ENL parameters. For instance, the porous layer of the sample

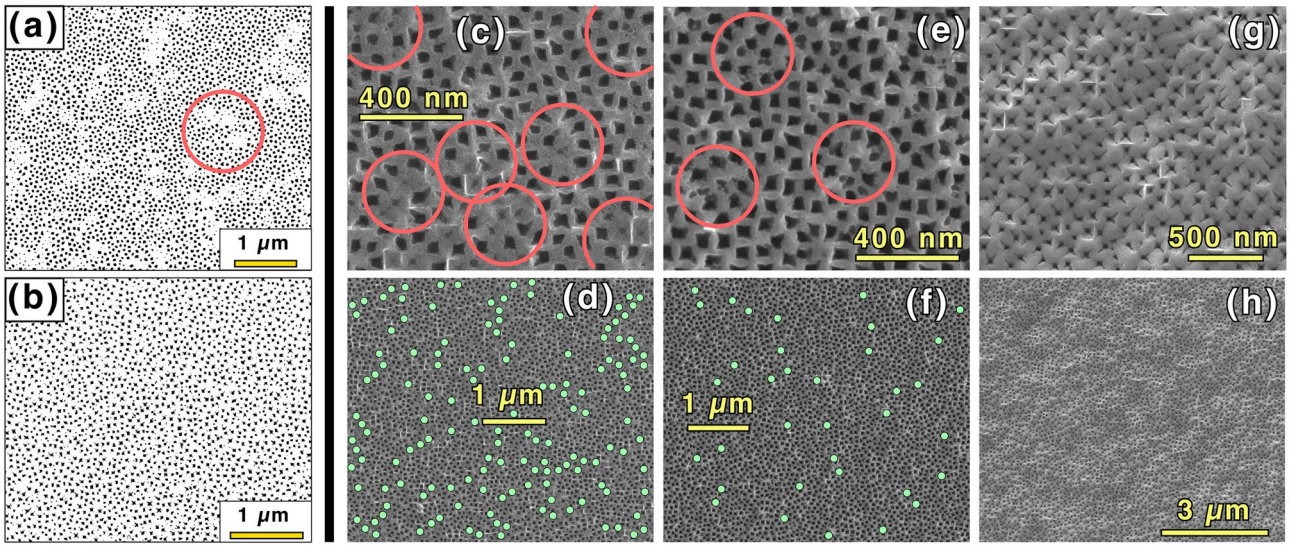


Fig. 10. Quantitative defect density evaluation via SEM top-view imaging on three different Si substrates with identical nominal specifications. (**a**, **b**) Thresholded top-view images of a defective (**a**) vs. optimal (**b**) substrates shown for reference. The red circle in (**a**) indicates one of the many defective areas where the pores are almost missing. No defective areas are visible in (**b**). (**c**–**h**) top views of samples from three separate wafer lots: defective (**c**, **d**), intermediate (**e**, **f**) and optimal (**g**, **h**). Top row (**c**, **e**, **g**) provides high-magnification images that evidence the morphology of defective areas (red circles). Bottom row (**d**, **f**, **h**) shows the corresponding large-area maps for defect counting, where green markers identify the defects positions. No defects are visible when using optimal wafers. Substrates (**c**, **d**) and (**g**, **h**) correspond to the same lots shown in Fig. 9, while the substrate in (**e**, **f**) is from a third lot. All three lots have a resistivity range within the 12–15 mΩ cm interval.

in (g) and (h) was fabricated using a lower current density with respect to the other two samples and shows, therefore, a smaller pore diameter. However, the porous layer after ENL was fabricated with the only aim of making the defects more clearly visible in SEM imaging, and a different pore size does not affect the measure. Using the size of the SEM surface images as a parameter, we can try to give an order-of-magnitude estimate of the method capability for the lowest defect density detection. Roughly, an SEM scan lateral size larger than 15 μm would reduce the image resolution below the limit for a reliable detection of a defective area. The lowest defect number counting being 1, we can assume that the detection limit is about 1 defect every 225 μm^2, that is about 5×10^5 defects/cm^2.

To evaluate the relevance of these defects, we note that the industrial standards[72,73] typically claim a defect range of about 0.3–0.5 defects/cm^2. In contrast, our results on defective substrates demonstrate a defect density ranging from 1×10^8 to 8×10^8 defects/cm^2, nine orders of magnitude higher than the industrial standard reference. These defects go unnoticed during standard industrial quality checks, and that makes them not only "unpredictable" but also "undetectable" by conventional procedures.

A direct measure of the consequences of the irregularities is shown in Fig. 11. The graphs shown are obtained using the methodology described in the work by E. Pinna et al.[26] and represent a measure of the distribution order of the pores opening on the samples' surface by means of an FFT of a thresholded SEM image. The left and center graphs show the FFT behavior for a low- and high-order samples, respectively. The graphs show that while for the sample reported on the left the interpore distance is regular up to the second nearest neighbor, for the samples reported on the center graph the interpore distance is regular up to the fifth nearest neighbor, which is a significant difference for many potential applications. The coincidence of the results for the two samples in the center graph indicate the high reproducibility of the ENL process. For comparison, the behavior of a porous layer prepared from a defective substrate is shown on the right graph. The correlation distance is poor even for the first nearest neighbor, with respect to the left graph sample. No effective control is possible on such defective substrates.

A further quantitative demonstration of the powerful control over the pores distribution that can be achieved by the ENL method is shown in Table 1. The pore densities are measured on different areas of a set of 2-inch porous layers formed after the ENL process. For all samples, the ENL process was performed using the same composition of the EC solution (21% HF), while the absolute formation currents used for the control of the densities of the indentations are indicated in the table for the L1 and L2 layers. The tight correlation between the L1 current and the final density is clearly demonstrated, together with the irrelevance of the current used for the L2 layer on the final pore density. Please note the homogeneity of the processing on the whole surface.

KPFM measurements

The identification of the small-scale inhomogeneities evidenced in this work is a very difficult challenge, as demonstrated by the fact that they stay unnoticed in the thorough ordinary investigations that are routinely

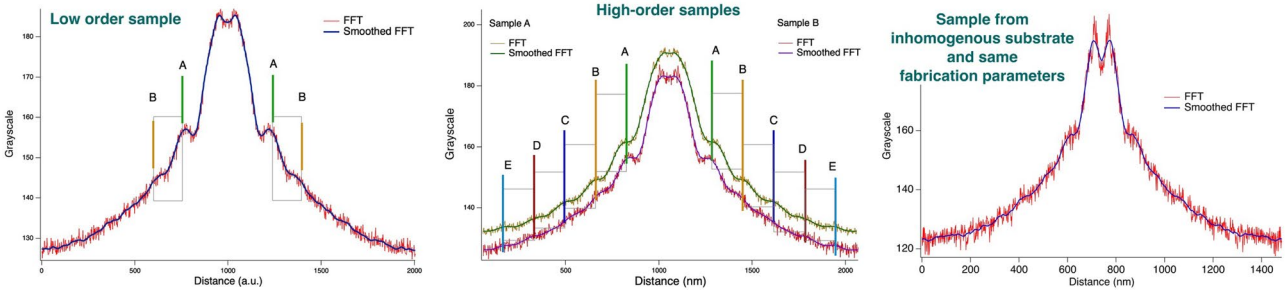


Fig. 11. Fast fourier transform plot from SEM top views of PSi samples formed after ENL. Left: a sample designed to have a low order distribution of pores. Center: two different samples designed for an improved order distribution. Right: a sample from a defective substrate: no effective control is possible.

Sample reference	L1 current (A) (density control)	L2 current (A) (order control)	Pores count	Sampling area (μm²)	Pore density (pores/μm²)	Average interpore distance (nm)	Mean pores/ μm²
1	6	16	3912	26.52	147	82	150 ± 5%
2	12	17	373	3.24	115	93	115 ± 5%
3		17	1395	12.96	108	96	
4a		14	1619	12.96	125	89	
4b		14	397	3.24	123	90	
5a		16	367	3.24	113	94	
5a		16	1486	12.96	115	93	
5a		16	5924	53.29	111	95	
5b		16	379	3.24	117	92	
5c		16	342	3.24	106	97	
6		14	2821	26.47	107	97	
7a	16	17	251	3.24	81	111	80 ± 5%
7a		17	1027	12.96	79	112	
7b		17	251	3.24	77	114	
7b		17	1003	12.96	77	114	

Table 1. Pores density control achieved using ENL on homogeneous 2-inch Si substrates. Labels "a", "b" or "c" after the sample's number in column 1 indicate different locations on samples surface. The current intensities used as control parameters of the ENL bilayer fabrication are indicated. These data, collected across multiple samples and surface areas, demonstrate both the process reproducibility and the high spatial homogeneity of the method. The statistical fluctuation in pore density (last column) is consistently within 5% of the mean values, based on extensive measurements across multiple samples from the optimal wafer lot.

performed for high-quality Si wafers. Standard Spreading Resistance Profiling (SRP)[74] lacks the necessary lateral resolution, as its millimeter-scale x-axis sensitivity is orders of magnitude larger than the observed defect spacing. Moreover, the higher z resolution is obtained through beveling. While on homogeneous substrates this approach gives an effectively improved spatial resolution, it has no impact on the real spatial resolution for small-volume defects as point defects. While Scanning Spreading Resistance Microscopy (SSRM)[74] and Kelvin Probe Force Microscopy (KPFM)[75] offer improved spatial and dopant resolution, SSRM requires high tip pressures (GPa range) that can induce surface damage, potentially artifacting the results since we are dealing with elusive inhomogeneities.

Analytical techniques such as Secondary Ion Mass Spectrometry (SIMS)[76], Micro-Raman[77], and Micro Photoluminescence (μPL) mapping[78] are similarly limited; they either lack the lateral resolution to resolve sub-100 nm variations or provide averaged signals that mask localized inhomogeneities. In the case of SIMS, the species diffusion induced by ion impacts can hinder small local dopant inhomogeneities that are among the possible causes for the effects we observe, unless maybe using very sophisticated tools as the Orbitrap™ SIMS[79]. Furthermore, although Transmission Electron Microscopy (TEM) and Scanning TEM with Energy Dispersive Spectroscopy (STEM-EDS) provide exceptional structural detail, their chemical sensitivity, typically limited to 0.1–0.5 wt%[80], is often insufficient to detect the subtle dopant fluctuations or small clusters influencing the electrochemical process. This is also true for TEM-derived techniques as Electron Tomography.

We estimated that KPFM was among the most suitable techniques to try to investigate the nature of the Si wafer inhomogeneities. Therefore, we performed a series of measurements on the sample from Fig. 7.

The results, shown in Fig. 12, compare AFM topographies (left) with KPFM potential maps (right) on the same areas. Panels (a–d) show cross-sectional views at the porous/bulk Si interface, while (e–f) show the top surface. The porous side is on the right side of panels (a–d). The KPFM measurements, obtained with a 30 nm tip radius at a 50 nm lift height, yield a lateral resolution of approximately 40–50 nm, matching the expected scale of the inhomogeneities. The relatively rough topography of the porous region in (a) and (c) hinders the detection of possible charge density variations in (b) and (d). The surface pore openings in (e, f) are however clearly visible as colored dots. The bulk Si side appears flat in both AFM and KPFM imaging. The observation that the bulk Si region appears homogeneous within a $\pm$ 20 mV range does not imply an absence of local charge density variations but rather establishes an upper limit for them. Based on these data and on the nominal dopant concentration of 2–3 $\times$ 10^{18} atoms/cm^3, local dopant fluctuations below a factor of $\pm$ 2.5 would remain undetected by KPFM (see Section "Kelvin Probe Force Microscopy (KPFM)"), yet they are sufficient to induce resistivity variations of over 30%. This confirms that the inhomogeneities are subtle enough to evade standard high-end metrology while remaining critical for electrochemical etching. These measurements further define the 'detection window' where only ENL is effective.

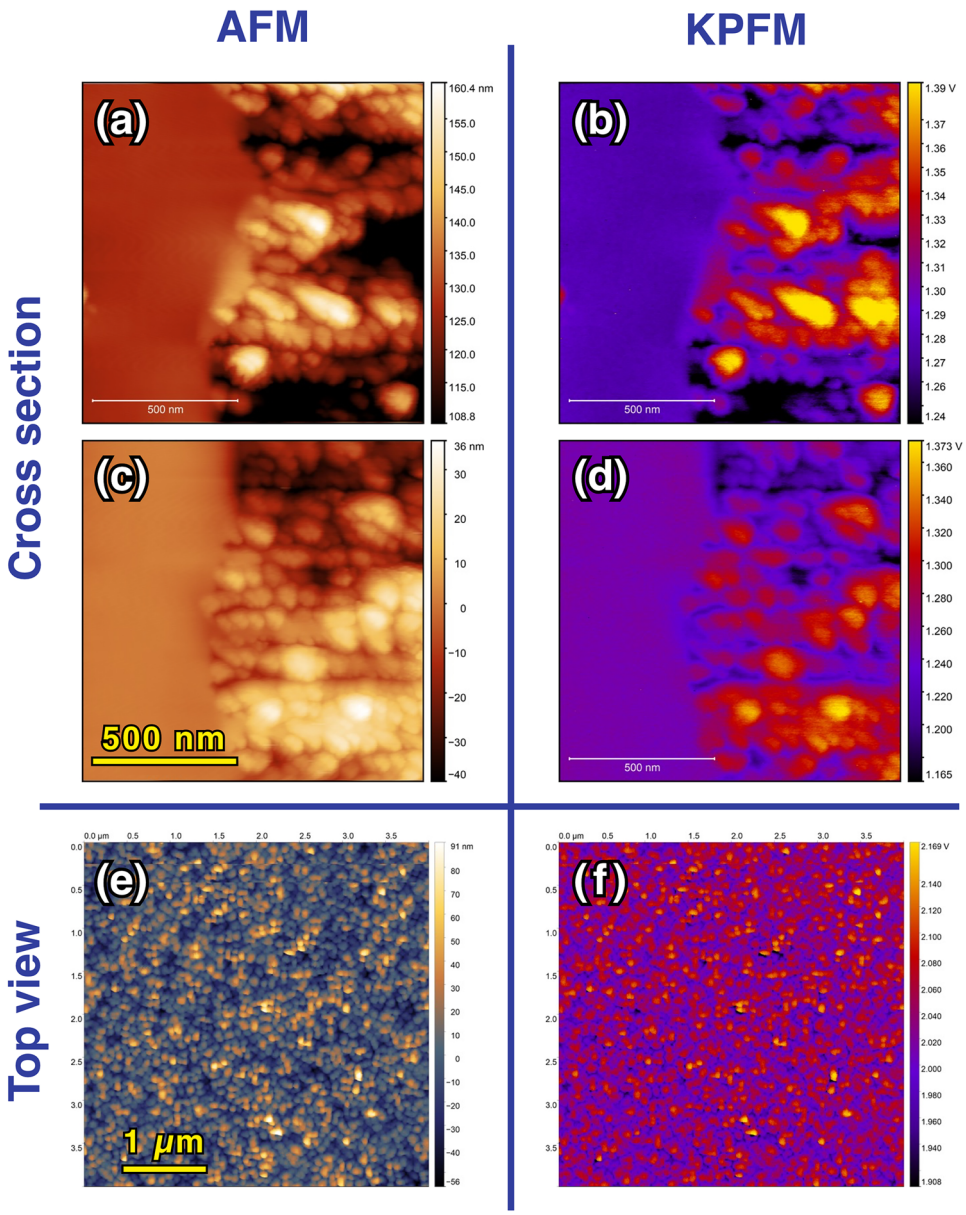


Fig. 12. AFM and KPFM measurements on the sample in Fig. 7. On the left side are the AFM topographies, while on the right side the KPFM measurements. (**a**, **b**) and (**c**, **d**) are two measurements on two different parts of the cross section, while (**e**, **f**) are a measurement on the top sample surface. (**a**, **b**) are over a more defective region whole (**c**, **d**) are on a more regular portion, as shown by the columnar pores.

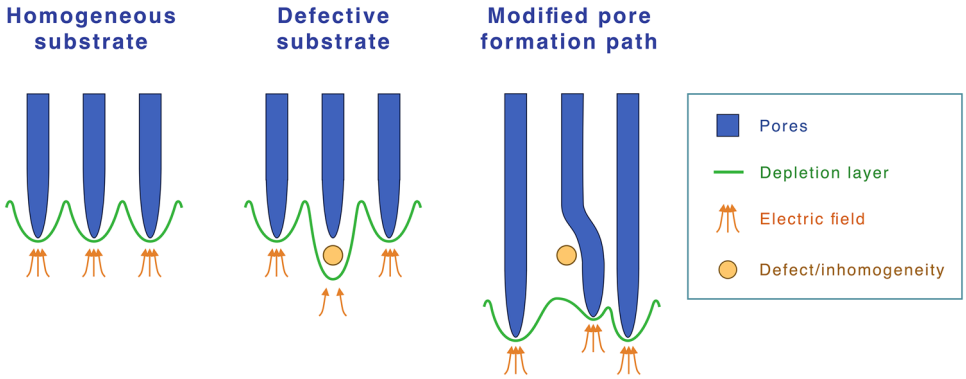


Fig. 13. – Schematic representation of the proposed pore propagation mechanism. The electric field (orange arrows) is enhanced at each pore's tip[86], enabling the tunneling current flow. The depletion layer front (green curve) and the electric field are regularly distributed in a homogeneous substrate (left), and a regular propagation front is produced. In a defective substrate (center), a defect (orange circle)) will induce a local widening of the barrier, creating a high-impedance domain. The local electric field will also be reduced, lowering the tunneling probability. This will cause a defect-induced deviation of the etching path (right): the formation current follows the path of least resistance, bypassing then the defect. The schematic is consistent with the experimental cross-sectional SEM observations.

Discussion

We already discussed the complexity of the CZ growth and the presence of large-scale defects as the ring defects. These defects typically induce only minor shape variations or smooth, millimeter-scale thickness fluctuations, both of which are difficult to detect via standard structural characterization on small areas (1 cm^2 or less) samples. The disruptions in porous layers regularity we observe here are instead due to small-scale defects/inhomogeneities whose characteristic dimensions are comparable to the pore diameter (<60 nm) as is the case of point defects[81]. These defects, likely vacancies[82], oxygen impurities[21,83], doping inhomogeneities[41], will impact the local strain field, the carrier mobility and the local electric field, therefore modifying the pore propagation process at the nanoscale.

The maximum density of the defects we observed is relevant if we aim at homogeneous layers, up to 8 defects/μm^2 (8×10^8 defects/cm^2) from top view SEM images. Several literature publications indicate, for highly P doped Si, the presence of phenomena as the Ostwald ripening that lead to the formation of SiP precipitates around O precipitates[84]. The presence of these precipitates has been recently investigated by Transmission Electron Microscopy, whose images show that their size is comparable to the one we expect for the defects we observe here and can have an elongated shape[85]. Wu et al.[85] also show experimentally that there is a direct correlation between the overall carrier concentration and the density of this SiP precipitates. This correlation strongly suggests that localized carrier density fluctuations modulate the local electric field nearby the inhomogeneities during the pore propagation process and, therefore, the local direction of the electrochemical etching. The defect density in Wu et al. work ($\approx 10^9$ cm^{-3}) is lower than what we observe here. This suggests that multiple causes are possible, including small local increase/decrease of the dopant atoms numbers that, while affecting the local carrier density, would remain hardly detectable by structural or chemical analysis. The SEM images of our samples also show that there are different kinds of porous layer irregular shapes. In Fig. 6, the pore propagation is essentially blocked on specific locations of the wafer, while the defects in Fig. 7 suggest smaller inhomogeneities on a more vertical distribution that do not block the pore propagation but still dramatically affect the pore shape. It is also possible that the smaller inhomogeneities provoking the structural irregularities in samples as the one shown in Fig. 7 are not vertically extended but trigger some kind of permanent modification of the pores' formation from a vertical to a dendritic pore propagation.

To tentatively model the observed behavior, we can start by reminding that in an electrochemical process for pore fabrication in highly doped n^+ silicon, one of the main processes is related to the tunneling current flow at the pores' tips[86,87]. This is particularly true in high-current–density formation of PSi, where the high applied electric fields allow the charge carriers to overcome the depletion region in crystalline Si. Since the tunneling current intensity is exponentially dependent on the barrier height and thickness, relatively small fluctuations in one or both these factors may dramatically affect its value and, therefore, the pore propagation process.

A schematic of the expected effect is shown in Fig. 13. During the EC PSi formation, in a homogeneous Si wafer there will be a depletion layer similar to the one depicted in the left panel[86,87]. The presence of a charge carriers' distribution inhomogeneity (a structural defect, a SiP cluster, …) will affect the depletion layer thickness in front of the pore's tip (center panel) and lower the local electric field. Since the current flow is necessarily on paths of least resistance, the presence of inhomogeneities in the charge carriers' density will affect the local electrical resistivity and, therefore, the electrochemical etching path (right panel).

Given the high formation rates of the porous layer, as high as 600–700 nm/s, generated by the high current densities we used in this study, even a small defect-induced transient formation delay of just 0.1 s is large enough to shift the main formation front 70 nm away from the defect position, with the defective areas showing lower formation rates. This is fully consistent with what we observe in the SEM images, where the defective regions

are thinner than the regular areas, making this mechanism a probable explanation of the observed behavior. In summary, the SEM images of defective substrates reveal multiple small areas where the pore nucleation is inhibited, which strongly suggests the failure of the ENL indentations to favor the controlled localization of tunneling current-based EC corrosion process at the nanoscale level.

The origin of this phenomenon is likely a non-uniform distribution of the dopant that creates high-impedance domains where the localized widening of the depletion region, schematically shown in the central panel of Fig. 13, effectively shields the electric field enhancement typically provided by the ENL nano-indentations or, inside the layer, by the pores' tips. Consequently, the corrosion process is moved from a vertical pore propagation to a dendritic morphology, as confirmed by cross-sectional SEM analysis. It is worth noting that a peculiar dopant behavior has also been studied in the case of PSi formation from boron-doped Si wafers[88], where it was shown that B atoms remain beneath the pore surface. In such structures, the authors show that the PSi structure can behave as an electron donor or acceptor depending on the surface states, further demonstrating how the local chemical and potential environment exerts a profound influence on the local electrochemical behavior.

While the specific nature of these inhomogeneities remains to be definitively assessed, they are most likely acting as small-volume high-impedance domains. Our findings demonstrate the possible presence within CZ silicon ingots of overlooked high-density point-defect inhomogeneities that, while staying undetected by standard structural metrology, can trigger dramatic structural alterations of the PSi layers. These defects ultimately impose a transition from ordered vertical growth to a stochastic dendritic morphology that significantly compromises the final material quality.

Conclusions

We have demonstrated the dramatic impact of unpredictable inhomogeneities within nominally identical Si wafers on PSi fabrication process. These inhomogeneities are most likely point defects, a critical and unresolved issue that continues to challenge both scientific and industrial communities. Our findings suggest that the presence of these nearly undetectable, small-scale defects has been significantly underestimated, even if they critically dictate the reliability of PSi fabrication processes. We believe that this lack of substrate consistency poses a substantial barrier to the industrial viability of numerous PSi applications when transitioning from laboratory prototypes to large-scale production, especially considering the relevance of the defect densities measured here, that exceed industrial standards by several orders of magnitude. In addition, the lack of reproducibility when using inhomogeneous substrate lots can lead to unforeseen setbacks in research projects. Our results clearly highlight how heavily small-scale inhomogeneities can compromise the reliability of research results, however high the quality of the experimenters' work.

While inhomogeneities are a key concern in Si wafer production, restricted access to Proprietary industrial processing knowledge significantly limits the advancement towards fully homogeneous and reliable Si wafers production. A stronger partnership between PSi researchers and Si wafer producers would therefore be highly valuable for both sides and advisable for tackling this shared challenge.

Data availability

All data needed to evaluate the conclusions in the paper are present in the paper. Additional data related to this paper may be requested from the authors.

Received: 10 December 2025; Accepted: 9 April 2026
Published online: 16 April 2026

References

1. Skottvoll, F. S., Escobedo-Cousin, E. & Mielnik, M. M. The Role of Silicon Technology in Organ-On-Chip: Current Status and Future Perspective. *Adv. Mater. Technol.* **10**, (2025).
2. Giubileo, F. Current advances in nanoelectronics, nanosensors, and devices. *Nanomaterials* **14**, 1771 (2024).
3. Kang, D.-K., Corno, J. A., Gole, J. L. & Shin, H.-C. Microstructured nanopore-walled porous silicon as an anode material for rechargeable lithium batteries. *J. Electrochem. Soc.* **155**, A276 (2008).
4. Kulova, T. L., Skundin, A. M., Pleskov, Y. V., Terukov, E. I. & Kon'kov, O. I. Lithium insertion into amorphous silicon thin-film electrodes. *J. Electroanal. Chem.* **600**, 217–225 (2007).
5. Erwin, W. R. *et al.* Engineered porous silicon counter electrodes for high efficiency dye sensitized solar cells. *Nanomaterials for Energy Applications 2014 - Topical Conference at the 2014 AIChE Annual Meeting* 115 (2014).
6. Kawaura, H., Suzuki, R., Nagasako, N. & Oh-ishi, K. Scalable synthesis of porous silicon electrodes for lithium-ion batteries via acid etching of atomized Al–Si alloy powders. *J. Power Sources* **610**, 234739 (2024).
7. Feyzi, E. et al. A comprehensive review of silicon anodes for high-energy lithium-ion batteries: Challenges, latest developments, and perspectives. *Next Energy* **5**, 100176 (2024).
8. Ballif, C., Haug, F.-J., Boccard, M., Verlinden, P. J. & Hahn, G. Status and perspectives of crystalline silicon photovoltaics in research and industry. *Nat. Rev. Mater.* **7**, 597–616 (2022).
9. Teng, Q. et al. Reliability challenges in CMOS technology: A manufacturing process perspective. *Microelectron. Eng.* **281**, 112086 (2023).
10. MicroChemicals. Si wafers production and specifications. *Silicon wafer production specification* https://www.microchemicals.com/dokumente/application_notes/silicon_wafer_production_specification.pdf (2025).
11. Rougieux, F. E., Grant, N. E. & Macdonald, D. Impact of grown-in point-defects on the minority carrier lifetime in Czochralski-grown silicon wafers. *Energy Procedia* **60**, 81–84 (2014).
12. Cho, H.-J., Lee, B.-Y. & Lee, J. Y. The effects of several growth parameters on the formation behavior of point defects in Czochralski-grown silicon crystals. *J. Cryst. Growth* **292**, 260–265 (2006).
13. Effect of Horizontal Magnetic Field in Czochralski Silicon Growth. **401**, 2025 (2025).
14. Wang, J., Liu, Y. & Wei, X. Optimization of bulk microdefect performance in epitaxial silicon wafer. *J. Cryst. Growth* **637–638**, 127742 (2024).

15. Gräf, D. et al. Comparison of high temperature annealed Czochralski silicon wafers and epitaxial wafers. *Mater. Sci. Eng., B* **36**, 50–54 (1996).
16. Wafer World. Epitaxial vs. Standard Silicon Wafers: Which One Do You Need? https://www.waferworld.com/post/epitaxial-vs-standard-silicon-wafers-which-one-do-you-need (2025).
17. University Wafers. Epitaxial vs. Standard Silicon Wafers: A Complete Guide. https://www.universitywafer.com/compare-epitaxial-vs-standard-silicon-wafers.html.
18. Basnet, R. *et al.* Ring defects in n-type Czochralski-grown silicon: A high spatial resolution study using Fourier-transform infrared spectroscopy, micro-photoluminescence, and micro-Raman. *J. Appl. Phys.* **124**, (2018).
19. Hourai, M. *et al.* Defect behavior during growth of heavily phosphorus-doped Czochralski silicon crystals. I. Experimental study. *J. Appl. Phys.* **136**, (2024).
20. Chiou, H.-D. Phosphorus concentration limitation in Czochralski silicon crystals. *J. Electrochem. Soc.* **147**345. (2000).
21. Dubois, S., Han, W., Enjalbert, N., Danel, A. & Wang, Y. Spatial distribution of dopants and oxygen-related defects in antimony-doped Czochralski silicon. *Solar Energy Materials and Solar Cells* **292**, (2025).
22. Evers, J., Klüfers, P., Staudigl, R. & Stallhofer, P. Czochralski's creative mistake: A milestone on the way to the gigabit era. *Angew. Chem. Int. Ed.* **42**, 5684–5698 (2003).
23. Beach, W. P. *Understanding the Float Zone Method Find Out More About the FZ Wafer.* **33407**, 33407 (2025).
24. Hendawi, R. & Di Sabatino, M. Analyzing structure loss in Czochralski silicon growth: Root causes investigation through surface examination. *J. Cryst. Growth* **629**, 127564 (2024).
25. Sortland, Ø. S., Øvrelid, E. J., M'Hamdi, M. & Di Sabatino, M. Investigation of pinholes in Czochralski silicon ingots in relation to structure loss. *J. Cryst. Growth* **510**, 1–6 (2019).
26. Pinna, E. et al. Electrochemical nanolithography on silicon: An easy and scalable method to control pore formation at the nanoscale. *Materials* **12**, 2891 (2019).
27. Mula, G., Cara, E., Mehrabanian, M., Pinna, E. & Redolfi Riva, E. *Method for the fabrication of a porous semiconductor with controlled pores distribution - EP3540762.* (2020).
28. Markov, I. V. *Crystal Growth for Beginners* (World Scientific, 2017). https://doi.org/10.1142/10127.
29. Feigelson, R. S. Crystal growth history: Theory and melt growth processes. *J. Cryst. Growth* **594**, 126800 (2022).
30. Depuydt, B., Theuwis, A. & Romandic, I. Germanium: From the first application of Czochralski crystal growth to large diameter dislocation-free wafers. *Mater. Sci. Semicond. Process.* **9**, 437–443 (2006).
31. Wang, P. et al. Germanium-doped Czochralski silicon for photovoltaic applications. *Sol. Energy Mater. Sol. Cells* **95**, 2466–2470 (2011).
32. Rudolph, P. & Jurisch, M. Bulk growth of GaAs an overview. *J. Cryst. Growth* **198–199**, 325–335 (1999).
33. Sukhoveyev, V. A. et al. GaN 20-mm diameter ingots grown from melt-solution by seeded technique. *MRS Internet J. Nitride Semicond. Res.* **5**, 438–444 (2000).
34. Hruban, A., Dalecki, W., Nowysz, K., Strzelecka, S. & Gladki, A. Synthesis and crystallization of ZnSe by liquid encapsulation technique. in (eds. Zmija, J., Majchrowski, A., Rutkowski, J. & Zielinski, J.) 31–34 (1997). https://doi.org/10.1117/12.280736.
35. Hobgood, H. M., Swanson, B. W. & Thomas, R. N. Czochralski growth of CdTe and CdMnTe from liquid encapsulated melts. *J. Cryst. Growth* **85**, 510–520 (1987).
36. Müller, G., Métois, J.-J. & Rudolph, P. *Crystal Growth: From Fundamentals to Technology*. (Elsevier, 2004).
37. Menzel, R., Rost, H.-J., Kießling, F. M. & Sylla, L. Float-zone growth of silicon crystals using large-area seeding. *J. Cryst. Growth* **515**, 32–36 (2019).
38. Czochralski, J. Ein neues Verfahren zur Messung der Kristallisationsgeschwindigkeit der Metalle. *Z. Phys. Chem.* **92U**, 219–221 (1918).
39. Smirnova, O. V., Durnev, N. V., Shandrakova, K. E., Mizitov, E. L. & Soklakov, V. D. Optimization of furnace design and growth parameters for Si Cz growth, using numerical simulation. *J. Cryst. Growth* **310**, 2185–2191 (2008).
40. Hendawi, R., Schön, H. & Di Sabatino, M. Data analysis of industrial Czochralski process: Investigation of ingots with structure loss. *Sol. Energy Mater. Sol. Cells* **283**, 113438 (2025).
41. Zeng, Y., Chen, J., Ma, X., Zeng, Z. & Yang, D. Grown-in defects in heavily phosphorus-doped Czochralski silicon. *Physica B Condens. Matter* **404**, 4619–4621 (2009).
42. Subramanian, A. et al. Investigation of doping processes to achieve highly doped Czochralski germanium ingots. *J. Electron. Mater.* **52**, 5178–5188 (2023).
43. Kobeleva, S. P., Anfimov, I. M., Berdnikov, V. S. & Kritskaya, T. V. Possible causes of electrical resistivity distribution inhomogeneity in Czochralski grown single crystal silicon. *Mod. Electron. Mater.* **5**, 27–32 (2019).
44. Chen, S. et al. Melt convection and temperature distribution in 300 mm Czochralski crystal growth with transverse magnetic field. *J. Cryst. Growth* **591**, 126722 (2022).
45. Shiraishi, Y. et al. Growth of silicon crystal with a diameter of 400mm and weight of 400kg. *J. Cryst. Growth* **229**, 17–21 (2001).
46. University wafer. What size are silicon wafers? https://www.universitywafer.com/silicon-wafer-diameters.html.
47. WaferWorld. Si wafers explained. https://www.waferworld.com/post/understanding-silicon-wafers.
48. Haunschild, J., Reis, I. E., Geilker, J. & Rein, S. Detecting efficiency-limiting defects in Czochralski-grown silicon wafers in solar cell production using photoluminescence imaging. *Physica Status Solidi (RRL) – Rapid Research Letters* **5**, 199–201 (2011).
49. Le, T. et al. Industrial Czochralski n-type silicon wafers: Gettering effectiveness and possible bulk limiting defects. *Solar RRL* **8**, 1–6 (2024).
50. Mustonen, K., Lähteenmäki, J. P. & Savin, H. Detection of microcracks in Cz-Si wafer manufacturing by photoluminescence imaging. *Phys. Status Solidi A Appl. Mater. Sci.* **24**, 1–9 (2024).
51. Frank-Rotsch, C., Dropka, N., Kießling, F. M. & Rudolph, P. Semiconductor crystal growth under the influence of magnetic fields. *Cryst. Res. Technol.* **55**, 1–6 (2020).
52. Zhang, W. et al. Simulation of oxygen and carbon impurity transport during magnetically controlled Czochralski silicon growth. *AIP Adv.* https://doi.org/10.1063/5.0239067 (2025).
53. Rost, H.-J., Menzel, R., Luedge, A. & Riemann, H. Float-zone silicon crystal growth at reduced RF frequencies. *J. Cryst. Growth* **360**, 43–46 (2012).
54. Kravtsov, A., Krauze, A., Virbulis, J. & Chikvaidze, G. Reduction of aluminium contamination in electron-beam melting of feed rods for 300 mm FZ silicon crystal growth. *J. Cryst. Growth* **673**, 128390 (2026).
55. Wafer World. *Czochralski process vs Float Zone*. https://www.waferworld.com/post/czochralski-process-vs-float-zone (2025).
56. University Wafers. *How to prepare Si wafers*. https://www.universitywafer.com/how-to-prepare-silicon-wafers.html (2025).
57. TopSil. *Preferred Float Zone (PFZ) Silicon for Power Electronics*. https://www.topsil.com/wp-content/uploads/2023/05/pfz_application_notelong_version_september_2014.pdf (2014).
58. MicroChemicals. *Si Ingot Production Process for Wafers*. https://www.microchemicals.com/dokumente/application_notes/czochralski_floatzone_silicon_ingot_production.pdf (2025).
59. Schweizer, S. L., von Rhein, A., Geppert, T. M. & Wehrspohn, R. B. Reduced pore diameter fluctuations of macroporous silicon fabricated from neutron-transmutation-doped material. *physica status solidi (RRL) – Rapid Research Letters* **4**, 148–150 (2010).
60. Duun, S. *et al. Application Note Neutron Transmutation Doped (Ntd) Silicon for High Power Electronics*. 1–12 (2013).
61. Ager, J. W. Semiconductors: Isotope effects in solids. In *Encyclopedia of Condensed Matter Physics* 485–496 (Elsevier, 2024). https://doi.org/10.1016/B978-0-323-90800-9.00090-1.

62. Barber, R., Nguyen, Q., Brockman, J., Gahl, J. & Kwon, J. Thermal neutron transmutation doping of GaN semiconductors. *Sci. Rep.* **10**, 16295 (2020).
63. Mula, G. et al. Electrochemical impedance spectroscopy of oxidized porous silicon. *Thin Solid Films* **556**, 311–316 (2014).
64. Mula, G. et al. Characterisation of the doping of porous Si with Er through electrochemical impedance spectroscopy. *Chem. Eng. Trans.* **41**, 403–408 (2014).
65. Mula, G. et al. Controlling the Er content of porous silicon using the doping current intensity. *Nanoscale Res. Lett.* **9**, 332 (2014).
66. Giugni, A. et al. Hot electron nanoscopy and spectroscopy (HENs). In *Conductive Atomic Force Microscopy* 319–354 (Wiley, 2017). https://doi.org/10.1002/9783527699773.ch15.
67. Henning, A. K. et al. Two-dimensional surface dopant profiling in silicon using scanning Kelvin probe microscopy. *J. Appl. Phys.* **77**, 1888–1896 (1995).
68. Sailor, M. J. *Porous Silicon in Practice: Preparation, Characterization and Applications* (Wiley, 2011). https://doi.org/10.1002/9783527641901.
69. Lehmann, V., Stengl, R. & Luigart, A. On the morphology and the electrochemical formation mechanism of mesoporous silicon. *Mater. Sci. Eng. B. Adv. Funct. Solid-State Mater.* **69–70**, 11–22 (2000).
70. Mulè Stagno, L. A technique for delineating defects in silicon. *Solid State Phenom.* **82–84**, 753–758 (2001).
71. Obermeier, G., Hage, J. & Huber, D. Oxygen precipitation and denuded zone characterization with the electrolytical metal tracer technique. *J. Appl. Phys.* **82**, 595–600 (1997).
72. WaferPro. WaferPro Si wafer defect density. https://waferpro.com/why-silicon-wafer-thickness-matters/ (2024).
73. Wafer World. Wafer World Si wafer defect density. https://www.waferworld.com/post/deep-dive-on-quality-control-methods-during-wafer-manufacturing (2025).
74. Laskar, M. A. R. *et al.* The enduring legacy of scanning spreading resistance microscopy: Overview, advancements, and future directions. *Appl. Phys. Rev.* **12**, (2025).
75. Melitz, W., Shen, J., Kummel, A. C. & Lee, S. Kelvin probe force microscopy and its application. *Surf. Sci. Rep.* **66**, 1–27 (2011).
76. Lockyer, N. P. et al. Secondary ion mass spectrometry. *Nat. Rev. Methods Primers* **4**, 32 (2024).
77. Li, R. et al. High spatial resolution of topographic imaging and Raman mapping by differential correlation-confocal Raman microscopy. *Opt. Express.* **30**, 41447 (2022).
78. Chen, X. & Shao, J. Microscopic mapping of infrared modulated photoluminescence spectra with a spatial resolution of ~2 μm. *Rev. Sci. Instrum.* https://doi.org/10.1063/5.0244755 (2024).
79. Spampinato, V. et al. SIMS analysis of thin EUV photoresist films. *Anal. Chem.* **94**, 2408–2415 (2022).
80. Conconi, R., Ortega, M., Nieto, F., Buono, P. & Capitani, G. TEM-EDS microanalysis: Comparison between different electron sources, accelerating voltages and detection systems. *Ultramicroscopy* **276**, 114201 (2025).
81. Yang, D. & Ma, X. Defects and Impurities in Silicon Materials. In *Handbook of Integrated Circuit Industry* 1677–1695 (Springer Nature Singapore, 2024). https://doi.org/10.1007/978-981-99-2836-1_76.
82. Yamada-Kaneta, H. et al. Vacancies in CZ silicon crystals observed by low-temperature ultrasonic measurements. *Phys. B Condens. Matter.* **401–402**, 138–143 (2007).
83. Lin, W. & Stavola, M. Oxygen segregation and microscopic inhomogeneity in Czochralski silicon. *J. Electrochem. Soc.* **132**, 1412–1416 (1985).
84. Wu, D. *et al.* Comprehensive understanding on phosphorus precipitation in heavily phosphorus-doped Czochralski silicon. *J. Appl. Phys.* **134**, (2023).
85. Wu, D. *et al.* Mechanistic insight into competing precipitation behaviors of phosphorus and oxygen in heavily phosphorus-doped Czochralski silicon. *J. Appl. Phys.* **138**, (2025).
86. Searson, P. C. & Macaulay, J. M. The fabrication of porous silicon structures. *Nanotechnology* **3**, 188–191 (1992).
87. Searson, P. C., Macaulay, J. M. & Ross, F. M. Pore morphology and the mechanism of pore formation in n-type silicon. *J. Appl. Phys.* **72**, 253–258 (1992).
88. Garrone, E. et al. A nanostructured porous silicon near insulator becomes either a p- or an n-type semiconductor upon gas adsorption. *Adv. Mater.* **17**, 528–531 (2005).

Acknowledgements

GM warmly thanks Ian Burnett from Inseto UK Ltd for very useful discussions on wafers fabrication methods. Part of this work has been carried out at QR Labs INRiM.

Author contributions

GM and EC conceived of the presented research. FAP, MNA and GM fabricated the samples, while GL made the SEM measurements and provided critical feedback on the structural analysis. BT performed and analyzed the KPFM measurements. All authors thoroughly discussed the results. GM took the lead in writing the manuscript. All authors provided relevant feedback and helped shape the research, the analysis and the manuscript. All authors have given approval to the final version of the manuscript.

Funding

Part of this work was financially supported under the University of Cagliari PoC_UniCa_2022 NanoPSi project.

Declarations

Competing interests

The authors declare no competing interests.

Additional information

Correspondence and requests for materials should be addressed to G.M. or G.L.

Reprints and permissions information is available at www.nature.com/reprints.

Publisher's note Springer Nature remains neutral with regard to jurisdictional claims in published maps and institutional affiliations.

Open Access This article is licensed under a Creative Commons Attribution-NonCommercial-NoDerivatives 4.0 International License, which permits any non-commercial use, sharing, distribution and reproduction in any medium or format, as long as you give appropriate credit to the original author(s) and the source, provide a link to the Creative Commons licence, and indicate if you modified the licensed material. You do not have permission under this licence to share adapted material derived from this article or parts of it. The images or other third party material in this article are included in the article's Creative Commons licence, unless indicated otherwise in a credit line to the material. If material is not included in the article's Creative Commons licence and your intended use is not permitted by statutory regulation or exceeds the permitted use, you will need to obtain permission directly from the copyright holder. To view a copy of this licence, visit http://creativecommons.org/licenses/by-nc-nd/4.0/.

© The Author(s) 2026